

Dehui XU, Yuelin WANG, Bin XIONG, Tie LI

# MEMS-based thermoelectric infrared sensors: A review

© The Author(s) 2017. This article is published with open access at [link.springer.com](http://link.springer.com) and [journal.hep.com.cn](http://journal.hep.com.cn)

**Abstract** In the past decade, micro-electromechanical systems (MEMS)-based thermoelectric infrared (IR) sensors have received considerable attention because of the advances in micromachining technology. This paper presents a review of MEMS-based thermoelectric IR sensors. The first part describes the physics of the device and discusses the figures of merit. The second part discusses the sensing materials, thermal isolation microstructures, absorber designs, and packaging methods for these sensors and provides examples. Moreover, the status of sensor implementation technology is examined from a historical perspective by presenting findings from the early years to the most recent findings.

**Keywords** thermoelectric infrared sensor, CMOS-MEMS, thermopile, micromachining, wafer-level package

## 1 Introduction

Any object with a temperature above absolute zero generates infrared (IR) radiation, which has a frequency range of  $3 \times 10^{11}$ – $4 \times 10^{14}$  Hz and a wavelength of 0.75–1000  $\mu\text{m}$ . Thus, IR radiation is the electromagnetic wave radiation between visible light and microwave ranges. Both IR spectrum (i.e., wavelength range) and energy density (i.e., intensity of radiation) depend on object type, surface temperature, surface shape, and other factors. The ideal IR radiation object is called a “black body.” The relationship between IR radiation and temperature can be expressed by the Planck radiation formula.

An IR sensor is a light sensor that can respond to external IR radiation. IR sensors can be divided according to the detection mechanism into thermal and photon IR sensors [1]. In thermal IR sensors, IR radiation is absorbed

and converted into thermal energy; consequently, the temperatures of sensitive components increase. The magnitude of the IR radiation signal is measured on the basis of the increase in temperature. For photon IR sensors, the electronic state of the semiconductor materials changes when the detector absorbs photons, and this change results in photovoltaic or other phenomena. Compared with thermal IR sensors, photon IR sensors generally exhibit good performance and short response time. However, the noise in photon IR sensors increases exponentially with increasing ambient temperature. Thus, cooling systems are indispensable for IR photon sensors, thereby limiting the applications of IR photon sensors. Moreover, photon IR sensors only respond to the IR radiation with a specific wavelength because of the influence of the width of the semiconductor band gap. By contrast, thermal IR sensors can operate at room temperature without cooling owing to their temperature measurement mechanism. Thus, the manufacturing cost and operation difficulty of thermal IR sensors are reduced compared with IR photon sensors. In addition, thermal IR sensors can also respond to various wavelengths of IR radiation.

Thermal IR sensors are classified according to their working principle into thermoelectric, pyroelectric, and bolometer IR sensors [1]. The temperature change in thermoelectric IR sensors is converted to voltage signal output by the Seebeck effect. The temperature change in pyroelectric IR sensors is measured by the charge accumulation in the heated objects. The temperature change in bolometer IR sensors is measured by the electrical resistance of the sensors. At present, micro-machined thermopile IR sensors are used in many different applications, such as spectrometers, gas sensors, and remote temperature sensors, because of their inherent advantages, including insensitivity to ambient temperature, broad spectral response, and ease of operation. Consequently, considerable attention has been focused on micro-electromechanical systems (MEMS)-based thermoelectric (thermopile) IR sensors.

The present paper aims to provide an overview of MEMS-based thermoelectric IR sensors, with particular focus on sensor implementation, and describe the current

Received November 7, 2016; accepted February 10, 2017

Dehui XU (✉), Yuelin WANG, Bin XIONG, Tie LI  
Science and Technology on Microsystem Laboratory, Shanghai Institute of Microsystem and Information Technology, CAS, Shanghai 200050, China  
E-mail: [dehuixu@mail.sim.ac.cn](mailto:dehuixu@mail.sim.ac.cn)

status of MEMS IR sensors based on thermoelectric materials. Information on IR sensors strictly related to MEMS is provided in other recent review articles (e.g., Ref. [2]).

## 2 Physics

### 2.1 Principle

Figure 1 shows the connection between the absorber and two different thermoelectric Materials  $A$  and  $B$ , and the other ends of thermoelectric Materials  $A$  and  $B$  are open. When an IR radiation flux,  $\Phi_{\text{rad}}$ , is collected by the absorber, the thermocouple junction warms up because of the incident heat. Then, the temperature difference,  $\Delta T$ , between the connection point (hot junction) and heat sink (cold junction) stabilizes. The Seebeck effect generates a voltage between the open ends as follows:

$$V_{\text{out}} = (\alpha_A - \alpha_B)\Delta T, \quad (1)$$

where  $\alpha_A$  and  $\alpha_B$  are the Seebeck coefficients for thermoelectric materials  $A$  and  $B$ , respectively.

A thermopile is a series-connected array of thermocouples. Thus, the voltage generated by the thermopile IR detector is directly proportional to the number of thermocouples,  $N$ :

$$V_{\text{out}} = N(\alpha_A - \alpha_B)\Delta T = (\alpha_A - \alpha_B)\Delta T_{\text{total}}, \quad (2)$$

where  $\Delta T_{\text{total}}$  is the sum of the temperature differences in the thermocouples.

As shown in Fig. 2, the thermal losses in a MEMS-based thermoelectric IR sensor are classified into three types: Solid thermal conduction,  $G_{\text{solid}}$ ; gas convection,  $G_{\text{gas}}$ ; and thermal radiation,  $G_{\text{rad}}$ . Thus, the total thermal conductance between the hot junction and its surroundings,  $G_{\text{th}}$ , can be determined by [3,4]

$$G_{\text{th}} = G_{\text{solid}} + G_{\text{gas}} + G_{\text{rad}}. \quad (3)$$

Solid thermal conduction loss refers to the dissipation of heat through the solid suspended thermopile structure to the silicon substrate. The thermopile structure consists of a semiconductor thermocouple leg and a dielectric membrane; thus,  $G_{\text{solid}}$  can be derived by [5]

$$G_{\text{solid}} = N \frac{k_1 t_1 w_1}{l_1} + N \frac{k_2 t_2 w_2}{l_2} + \frac{k_3 t_3 w_3}{l_3}, \quad (4)$$

where  $k_n$ ,  $t_n$ ,  $w_n$ , and  $l_n$  denote the material conductivity, the layer thickness, the total width of the layer, and the length of layer ( $n = 1$  for n-type semiconductor thermocouple leg;  $n = 2$  for p-type semiconductor thermocouple leg;  $n = 3$  for the dielectric membrane), respectively.

MEMS-based thermoelectric IR sensors are generally packaged in atmospheric pressure packaging. The gas convection loss is due to the heat transport caused by the movement of molecules in air fluids. Thus,  $G_{\text{gas}}$  can be determined by [3,4]

$$G_{\text{gas}} = k_g A_s \left( \frac{1}{d_1 + 2 \frac{2-a}{a} \frac{m_0 p_0}{p}} + \frac{1}{d_2 + 2 \frac{2-a}{a} \frac{m_0 p_0}{p}} \right), \quad (5)$$

where  $k_g$  is the thermal conductivity of the atmospheric gas,  $A_s$  is the suspended area,  $d_1$  is the distance between the membrane and etching cavity bottom,  $d_2$  is the distance between the membrane and box cover of the package,  $a = 0.77$  is the accommodation factor representing the efficiency of the energy transmission between gas molecules [6],  $\frac{m_0 p_0}{p}$  is the mean free path of gas molecules,  $p$  is the pressure, and  $m_0 p_0 = 6.65 \times 10^{-3} \text{ Pa} \cdot \text{m}$  for nitrogen at room temperature.

Thermal radiation loss refers to the energy radiated from hot surfaces as electromagnetic waves. The temperature difference between the hot and cold junctions is considerably lower than the ambient temperature; thus, the thermal radiation loss can be derived by

$$G_{\text{rad}} = 4A_s \xi_{\text{eff}} \sigma_b T_0^3, \quad (6)$$

where  $\xi_{\text{eff}}$  is the effective emissivity coefficient of the thermopile structure and  $\sigma_b$  is the Stefan-Boltzmann constant.

### 2.2 Figures of merit

Responsivity ( $R_s$ , V/W) is a basic figure of merit for

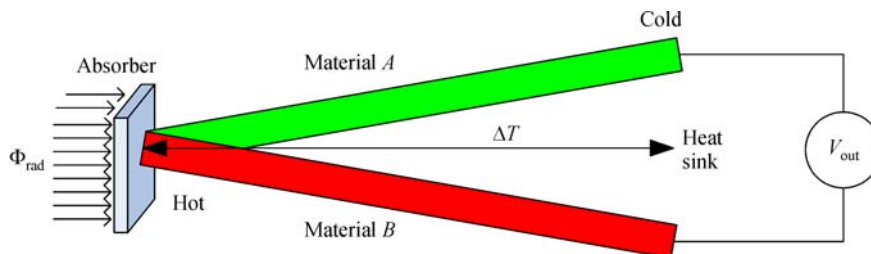


**Fig. 1** Working principle of a MEMS-based thermoelectric IR sensor: An output voltage,  $V_{\text{out}}$ , is generated when an IR radiation flux,  $\Phi_{\text{rad}}$ , irradiates on the sensor

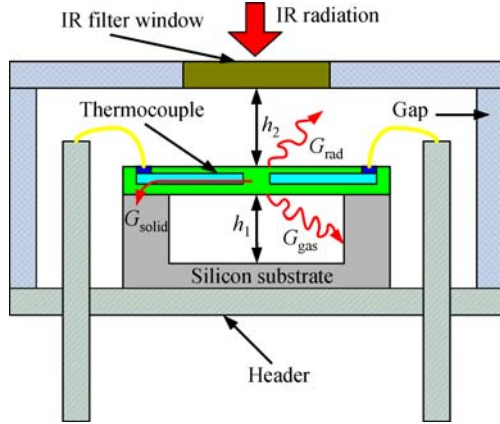


**Fig. 2** Cross-sectional view of a MEMS-based thermoelectric IR sensor (solid thermal conduction, gas convection, and thermal radiation are the thermal transport mechanisms of this IR sensor)

thermoelectric IR sensors. It is the ratio of output voltage ( $V_{out}$ ) to incident IR power, and can be expressed as

$$R_s = \frac{V_{out}}{A_{abs} \Phi_{in}} = \frac{N \alpha_{AB} \eta}{G_{th}}, \quad (7)$$

where  $A_{abs}$  is the absorber area of the IR sensor,  $\Phi_{in}$  is the IR power density,  $N$  is the number of thermocouples,  $\alpha_{AB}$  is the Seebeck coefficient of the thermocouple,  $\eta$  is the absorption of the absorber layer, and  $G_{th}$  is the total thermal conductance between the hot junction and its surroundings.

Specific detectivity ( $D^*$ ,  $\text{cm} \cdot \text{Hz}^{1/2}/\text{W}$ ), which allows the comparison of IR sensors with different absorber areas and sensor technologies, is determined by

$$D^* = \frac{R_s \sqrt{A_s \Delta f}}{u_{noise}}, \quad (8)$$

where  $\Delta f$  is the measurement frequency bandwidth and  $u_{noise}$  is the noise voltage of the thermopile IR detector. Johnson noise dominates  $u_{noise}$ ; thus,  $u_{noise}$  can be written as

$$u_{noise} = \sqrt{4kRT \Delta f}, \quad (9)$$

where  $k$  is the Boltzmann constant,  $R$  is the electrical resistance of the detector, and  $T$  is the absolute environment temperature.

Many studies [5,7–16] have been conducted on the analytical modeling of MEMS-based thermoelectric IR sensors. Völklein and Baltes [8] proposed a 1-D analytical model on the assumption that temperature is uniform over the absorber area. Kozlov [9] used a 1-D two-zone model to optimize a thermoelectric radiation sensor with a separate thermoelectric transducer. Socher et al. [6,7] applied an optimization methodology to front-etched cantilever and bridge-type thermopile IR sensors with a close-membrane structure. Kozlov [10,11] used a Fourier model for the steady-state temperature distribution and

frequency response of thermal microsensors. Escriba et al. [13] employed a 1-D three-zone model that considers the hot junction as a single zone to simulate a back-etched micromachined thermopile IR detector. Xu et al. [5] established an analytical model for a complementary metal oxide semiconductor (CMOS)-MEMS thermoelectric IR sensor with a front-etched structure and found that the largest errors between the simulation values and the experimental data are 5.7% and 6.6% for sensitivity and detectivity, respectively, when the IR absorption in the thermocouple area is considered.

### 3 Sensor implementation

In recent decades, MEMS-based thermoelectric IR sensors have experienced rapid developments because of the advances in micromachining technology. Lahiji and Wise [17] reported a micromachined thermoelectric IR sensor in the early 1980s. The thermocouple composition consists of Bi-Sb and Si-Au. For MEMS-based thermoelectric IR sensors, the manufacturing cost of the sensor can be reduced by micromachining, and the sensor performance can be further improved by microthermal isolation.

#### 3.1 Thermoelectric material

Thermoelectric materials determine the Seebeck coefficients of thermocouples. The figure of merit of thermoelectric materials,  $Z$ , is characterized by electrical resistivity  $\rho$ , thermal conductivity  $\lambda$ , and thermoelectric power  $\alpha$  and is defined as [18]

$$Z = \frac{\alpha^2}{\rho \lambda}. \quad (10)$$

Table 1 [18,19] summarizes the typical values of the thermoelectric parameters of the most widely used materials for MEMS-based thermoelectric sensors. Chemical compounds are often used to improve thermoelectric performance. By using  $\text{Bi}_{0.87}\text{Sb}_{0.13}$  (n-type) and Sb (p-type) as the combination of thermoelectric materials, Haenschke et al. [20] developed a thermoelectric IR sensor with  $D^*$  greater than  $2 \times 10^9 \text{ cm} \cdot \text{Hz}^{1/2}/\text{W}$ . Although silicon and polysilicon are not high-performance thermoelectric materials, they are widely adopted as thermoelectric sensing materials in MEMS-based thermoelectric IR sensors because of their good CMOS compatibility. CMOS-compatible IR sensors can easily be scaled down and produced by cost-efficient standard CMOS processes. Moreover, metal-metal thermocouples are preferable to semiconductor thermocouples for MEMS-based thermoelectric IR sensors because of the good compatibility of these thermocouples with micromachining and microelectronic technologies [21].

**Table 1** Properties of thermoelectric materials for MEMS-based thermoelectric IR sensor [18,19]

Material	Doping type	Seebeck coefficient $/(\mu\text{V}\cdot\text{K}^{-1})$	Electrical resistivity $/(\mu\Omega\cdot\text{m})$	Thermal conductivity $/(W\cdot\text{m}^{-1}\cdot\text{K}^{-1})$	Figure of merit $/(10^{-3}\text{K}^{-1})$	Doping concentration $/(10^{20}\text{cm}^{-3})$
$\text{Bi}_2\text{Te}_3$	n	-240	10	2.02	2.89	0.23
$\text{Bi}_2\text{Te}_3$	p	162	5.5	2.06	2.32	2.55
PolySiGe	n	-136	10.1	4.45	0.328	1–3
PolySiGe	p	144	13.2	4.80	0.413	2–4
PolySi	n	-120	8.5	24	0.071	3.4
PolySi	p	190	58	17	0.037	1.6
Si (SOI)	n	-239	7.1	/	/	/
Si (SOI)	n	-192	2.6	/	/	/
Si (SOI)	n	-236	2.5	/	/	/
Si (SOI)	n	-198	5.5	/	/	/

### 3.2 Thermal isolation

Thermal isolation induces the temperature difference across the sensing structure. Thus, thermal isolation is a key factor in MEMS IR sensors. A typical method for thermal isolation is etching the silicon substrate beneath the thermopile microstructure. Figure 3 depicts two different thermal isolation structures reported in the literature. The respective silicon substrates are etched either on the back side [22–27] or on the front side [28–31].

#### 3.2.1 Back-side etching

In the back-etched thermoelectric IR sensor, the entire bulk silicon is removed on the back side by wet anisotropic etching or deep reactive ion etching (DRIE). In early studies, back-side wet anisotropic micromachining is always selected for releasing thermopile structures [32]. KOH wet etching and tetramethylammonium hydroxide (TMAH) wet etching are two common methods for wet anisotropic micromachining. By using silicon on the insulator substrate and TMAH etching, Müller et al. [23] demonstrated the integration of the IR sensor and circuit; p-Si and n-polysilicon were adopted as the thermocouples, and TMAH etched the silicon substrate and stopped at the buried oxide layer in the thermal isolation. Sarro et al. [24] demonstrated a p-Si/Al thermoelectric IR sensor fabricated

by self-stop silicon etching by heavily doping the substrate beneath the structure. However, approximately 10  $\mu\text{m}$  doping silicon film is left after the structure release; consequently, thermal isolation was restricted.

The entire silicon substrate is removed in back-etched thermoelectric IR sensors; thus, the front-side microstructures are difficult to protect because of the long silicon etching time. Back-side wet anisotropic etching also limits the size of the device, because of the angle of the anisotropic etching. Furthermore, using double-sided lithography in back-side micromachining induces process complications. Moreover, a stiction problem due to capillary forces in wet etching leads to a decreased release yield. Compared with wet anisotropic etching, DRIE offers such advantages as dry etching, large etch rate, small chip size, and improved CMOS compatibility. Nevertheless, DRIE-based micromachining causes plasma damage and increases the thermal budget [32]. Furthermore, DRIE is more costly than wet anisotropic etching.

#### 3.2.2 Front-side etching

In front-etched micromachined sensors, the bulk silicon is partially removed on the front side by etching windows in the structure layers. The device structure can be released by wet anisotropic etching, DRIE, or  $\text{XeF}_2$  etching. Only a part of the silicon substrate is removed; thus, the microstructure can be released within a short time.

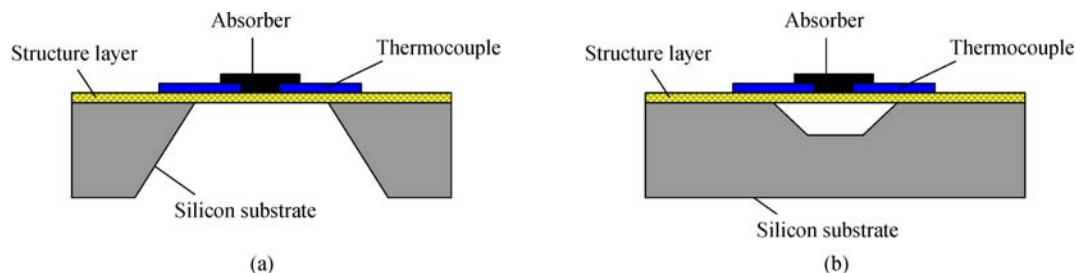


**Fig. 3** Two reported thermal isolation structures: (a) Back-etched thermal isolation structure; (b) front-etched thermal isolation structure

Moreover, a smaller device structure can be realized, and only one-side lithography is used for the sensor process because the microstructure is fabricated on the front side. These advantages result in improved CMOS compatibility and low fabrication cost. Thus, front-side etching thermal isolation is widely adopted in CMOS-MEMS thermoelectric IR sensors.

In the 1990s, comparative studies on front-side etching CMOS-MEMS thermoelectric IR sensors were conducted [28–31]. Polycrystalline silicon and aluminum, which are common materials in the CMOS process, were used as the thermocouples, and an IR sensor and a readout circuit were integrated. The sensor structure was released from the front side by TMAH etching. To release the sensor structure within a short time, a cantilever beam structure was adopted, thereby reducing the mechanical stability and sensitivity.

Du and Lee [4] and Li et al. [33] achieved a close-membrane microstructure for IR sensors by front-side TMAH etching and consequently improved mechanical stability. A [100] direction window for anisotropic etching is faster than a [110] direction window on a (100) Si wafer. If [100] direction windows are properly distributed, the etching time for a membrane will be significantly shortened. However, given that TMAH etching is a wet process, the close-membrane structure also suffers from the stiction problem.

In view of the anisotropic nature of TMAH etching, the placement options for the etching windows are limited. For a short release time, the etching windows cut off the heat transfer path from the absorber to the hot junctions. As shown in Fig. 4, the temperature difference across the

thermocouple can be improved by 70% by changing the placement of the etching windows. Xu et al. [34] developed a thermoelectric IR sensor by  $\text{XeF}_2$  front-side isotropic etching. The isotropic etching features increase the placement options for the etching windows [35]. Figure 5(a) [36] shows the etching window design for a thermoelectric IR sensor, in which the etching windows are designed to avoid cutting off the heat transfer path from the absorber to the hot junctions and improve the temperature difference across the thermocouple. Moreover, the releasing evolution is also predicted in Fig. 5(a). The time etching evolution of isotropic silicon etching by  $\text{XeF}_2$  is illustrated in Figs. 5(b) and 5(c). The time etching evolution is as predicted in Fig. 5(a). Figure 5(d) shows the scanning electron microscope (SEM) of the IR sensor structure after  $\text{XeF}_2$  front-side etching. The etching window design in the absorber and the thermocouple improves the thermal isolation of the microstructure.

As a silicon etchant,  $\text{XeF}_2$  presents unique advantages, such as high selectivity for silicon, gas phase isotropic etching, and ease of operation. Thus,  $\text{XeF}_2$  etching can avoid the stiction problem in the wet etching process and the plasma damage in the DRIE process; consequently,  $\text{XeF}_2$  etching is suitable for CMOS-MEMS thermoelectric IR sensors. Xu et al. [36] developed a CMOS-MEMS thermoelectric IR sensor by  $\text{XeF}_2$  front-side isotropic etching; the maximum transconductance change of the CMOS device after  $\text{XeF}_2$  etching was 1.25%.

As suggested in Eq. (5), a larger gap beneath the sensor structure leads to a smaller  $G_{\text{gas}}$ , that is, a better sensor performance.  $G_{\text{gas}}$  in back-side etching thermal isolation is smaller than that in front-side etching thermal isolation, in

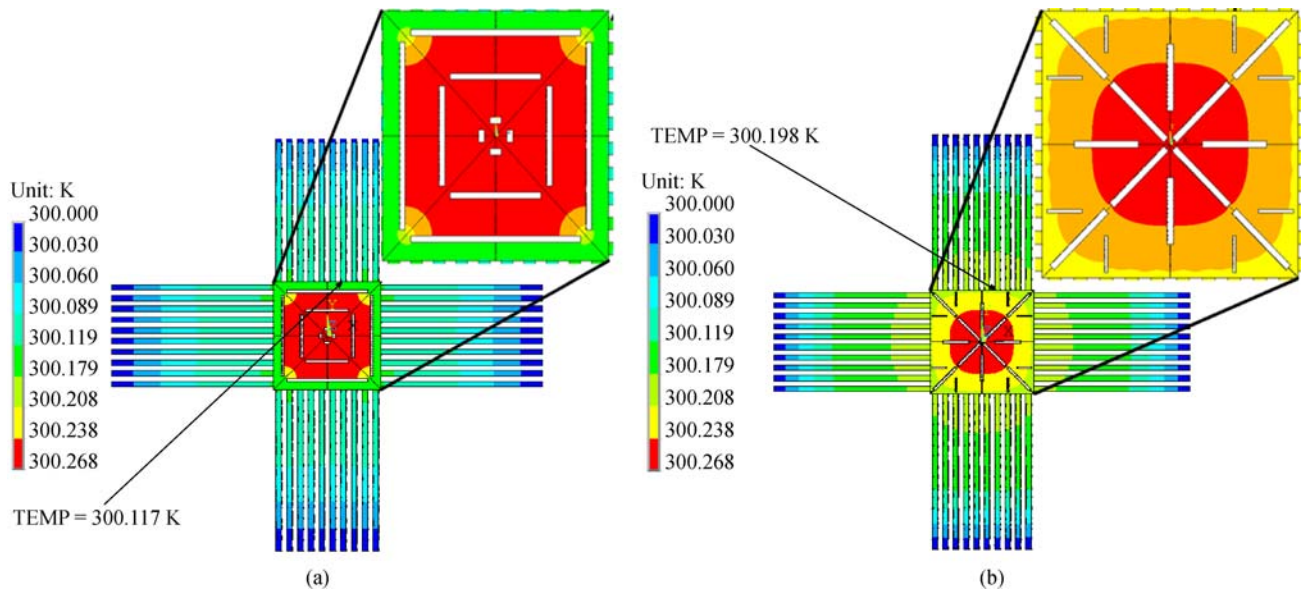


**Fig. 4** FEM-simulated temperature distribution in the IR sensor microstructure with different etching window placement designs. The inset picture presents the temperature distribution in the absorber area, in which the white etching window design is clearly shown. The hot junction temperature is also indicated with an arrow. (a) The etching windows cut off the heat transfer path from the absorber to the hot junctions; (b) the etching windows avoid cutting off the heat transfer path from the absorber to the hot junctions

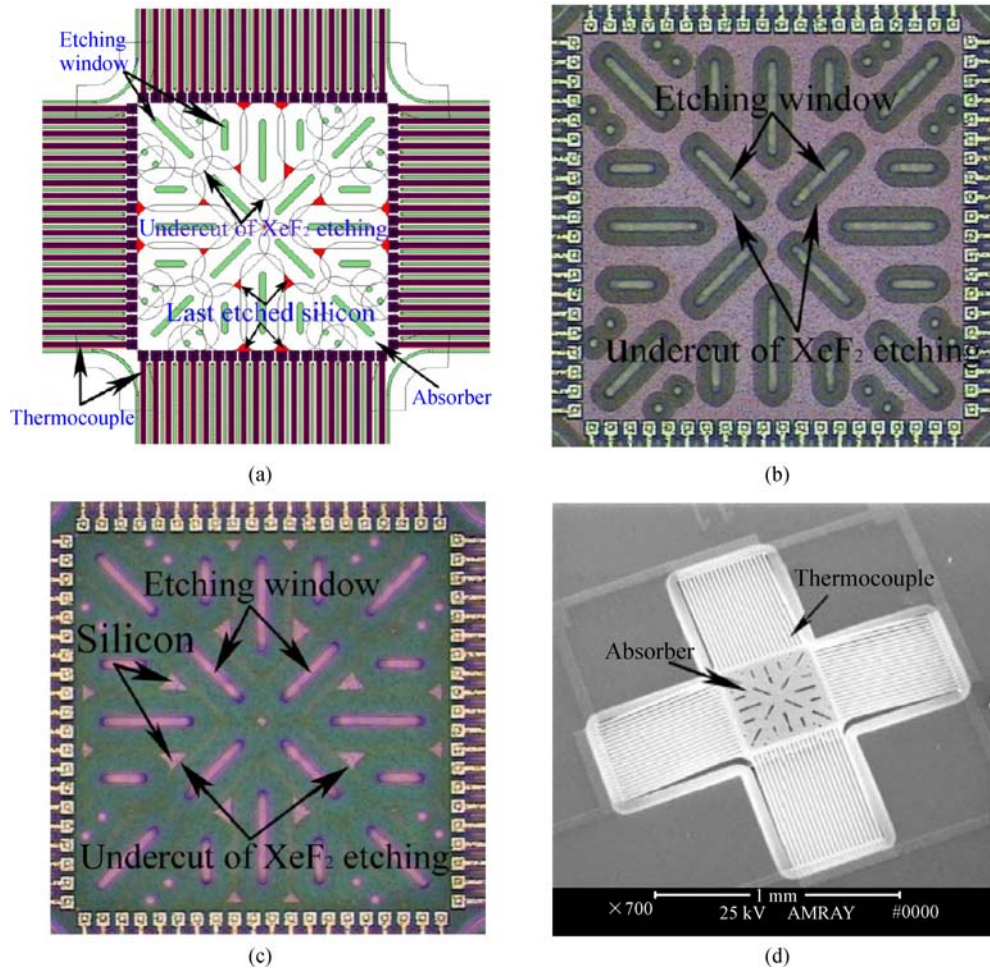


**Fig. 5** (a) Layout design of the etching windows of a thermoelectric IR sensor released by XeF<sub>2</sub> etching. The last etched silicon by XeF<sub>2</sub> etching is predicted from the layout design: The optical micrograph of the etching window design after (b) 40 and (c) 90 cycles of XeF<sub>2</sub> etching. (d) SEM picture shows the structure of the thermoelectric IR sensor and etching window design [36]

which the gap beneath the sensor structure is less than 100  $\mu\text{m}$ . Thus, front-side etching thermoelectric IR sensors usually show poor performance. However, combining back-side etching and front-side etching can improve the sensor performance twice as high as that of front-side etching alone [37]. Figure 6 presents the sensor structure when the front-side etching and back-side etching are combined. First, wet anisotropic pre-etching forms a cavity on the back side. Then, a front-side XeF<sub>2</sub> isotropic post-etching removes the rest of the silicon and releases the microstructure.

### 3.3 Infrared absorption

The performance of thermoelectric IR sensors can be calculated by IR-heat and heat-voltage two-stage conversion [1]. As suggested in Eq. (7), the IR absorption efficiency must be high, and the thermal mass of the absorption layer must be low to achieve high sensitivity. In general, IR radiation absorbers can be divided into four

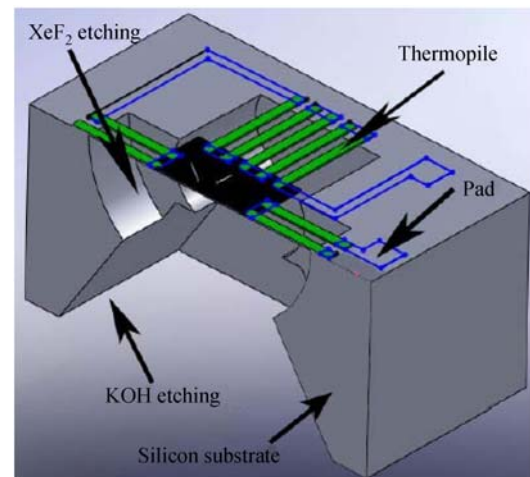


**Fig. 6** Cross-section of the thermoelectric IR sensor fabricated by combining back-side etching and front-side etching

groups: Thin interferometric microstructure [38], porous metal black [39], passivation thin film [33–37], and thick silicon layer [25–27].

Absorbers based on thin interferometric microstructures comprise three stacked layers. IR absorption occurs due to the destructive interference of the reflected and incident waves. By varying the thicknesses of the three layers, the absorption spectrum of the interferometric absorber can be aligned to the desired wavelength. However, such absorbers possess a narrow spectral bandwidth. A maximum absorption of 91% was in the 3–5  $\mu\text{m}$  wavelength range [38].

Porous metal black absorbers can be fabricated by electroplating and evaporation. Platinum-black is usually deposited by electroplating. In comparison, gold-black, silver-black, aluminum-black, and bismuth-black are evaporated in a low-pressure process under nitrogen atmosphere. The absorption coefficient of porous metal blacks is remarkably high (approximate to 1) along the entire wavelength (from a very short wavelength up to more than 10  $\mu\text{m}$ , thus including both atmospheric windows). Porous metal black absorbers must have a dendritic, soft structure to attain the desired absorption properties; thus, they are very fragile and easily destroyed by contact.

As absorbers, CMOS passivation thin films fully exploit the potential of the CMOS process and reduces fabrication complexity because both  $\text{SiO}_2$  and  $\text{Si}_3\text{N}_4$  thin films are available in the CMOS-MEMS process. The IR absorption of the passivation layer depends on the chemical bond IR absorption. A passivation layer allows for a mean absorption of 70% in the 9–13  $\mu\text{m}$  wavelength range because of the diffraction effects [34].

Si exhibits IR absorption in the mid-IR wavelength, a thick bulk silicon layer has been reported as an IR absorber in the literature. Silicon IR absorbers present robustness and good CMOS compatibility. However, they require the minimum thickness for a sufficient optical path for IR absorption. Thus, the thermal mass of the device is significantly increased by the absorber; consequently, the sensitivity is deteriorated.

### 3.4 Package

Packaging is a core technology for leveraging the functions and performances of sensing structures in a system. For MEMS-based thermoelectric IR sensors, the packaging must realize two purposes. First, because the sensing microstructure is a thin film structure with a thickness of less than 5  $\mu\text{m}$ , the packaging must protect the fragile membrane microstructure from mechanical damage, dust, and fingerprints to ensure long-term stability and reliability. Second, the packaging must select the working IR wavelength for the IR sensor. Packaging methods for thermoelectric IR sensors can be divided into three types, namely, TO-CAN packaging, flip chip packaging, and

wafer-level packaging.

Widely used for thermoelectric IR sensors, TO-CAN packaging involves dicing up the device wafer and mounting the IR sensor die on a metal TO transistor baseplate. Then, a metal TO transistor cap with an attached optical filter hermetically seals the sensor chip. The packaged device usually has a large dimension because of the metal TO transistor house.

Flip chip packaging assembles the IR filter on top of the IR sensor by a flip chip technique [25–27]. The device size is considerably reduced because the metal can house is not adopted. However, both TO-CAN and flip chip packaging are component-level packaging methods, which are characterized by low efficiency and high cost.

Wafer-level packaging can encapsulate and protect the microstructure of the device prior to dicing as well as reduce the size and cost [40–42]. Moreover, vacuum packaging can be realized by vacuum bonding. As shown in Eq. (5), vacuum packaging is ideal for eliminating  $G_{\text{gas}}$  in thermoelectric IR sensors. Figure 7 shows a comparison of component-level and wafer-level packaging methods. In the wafer-level packaging, the IR sensor dies are vacuum-sealed at the wafer level by a single vacuum bonding process. Then, the wafer is diced into individually packaged dies. The packaging efficiency is improved, and the packaging cost is reduced because packaging is performed at the wafer level. Compared with the component-level packaging method, wafer-level packaging has the advantages of low cost, high volume throughput, and miniaturization.

Xu et al. [43,44] developed a wafer-level packaged thermoelectric IR sensor. The IR sensors were vacuum-sealed with a filter cap wafer by an Au-Au thermocompression vacuum bonding method using sputtered Au layers. The reliability of the wafer-level packaged IR sensor satisfied the MIL-STD-883E requirements. The responsivity and specific detectivity of the wafer-level vacuum packaged IR sensor exhibited fourfold increases compared with the same IR sensor in atmospheric pressure packaging. Figure 8 presents the sensor after wafer-level packaging. The sensor fabrication and packaging are wafer-level processes; thus, the sensor is suitable for batch fabrication process.

---

## 4 Conclusions

The status of MEMS-based thermoelectric IR sensors has been reviewed to provide an overview of thermoelectric IR sensor theory, fabrication, and packaging. This review posits that thermoelectric IR sensors can evolve into an IR system on chip both in the planar direction by CMOS-MEMS technology and in the vertical direction by wafer-level packaging. Moreover, CMOS-MEMS thermoelectric IR sensors can be fabricated through conventional CMOS processes. This fabrication mode can pave the way for

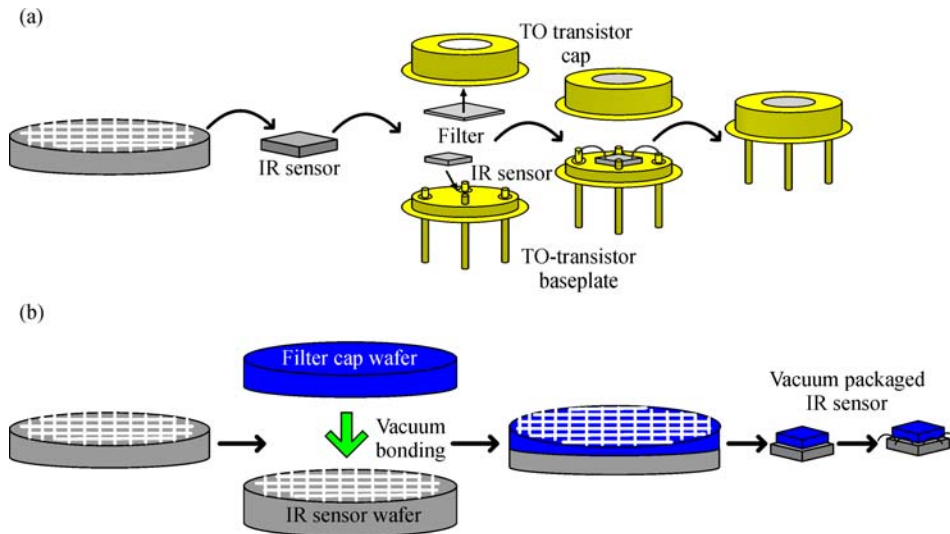


**Fig. 7** Comparison of component-level and wafer-level vacuum packaging methods for MEMS-based thermoelectric IR sensors. (a) Component-level packaging; (b) wafer-level packaging

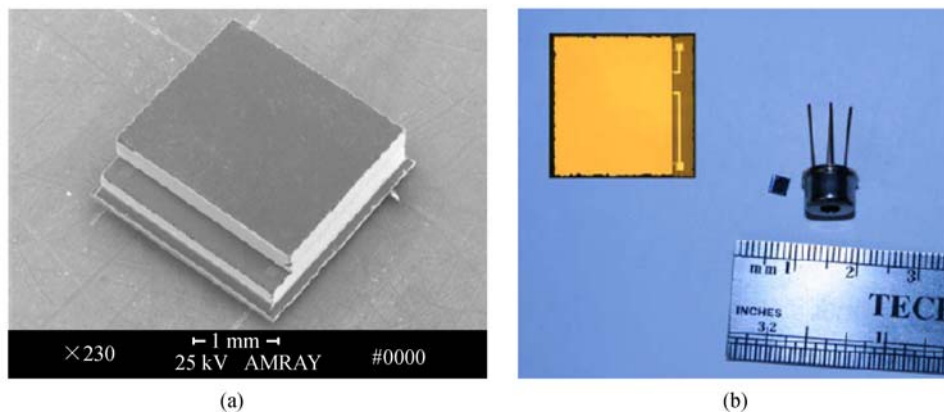


**Fig. 8** (a) SEM of wafer-level packaged IR sensor; (b) optical graphic of the wafer-level packaged thermoelectric IR sensor compared with its TO transistor packaged counterpart, with the upper-left figure showing the magnified top view of the wafer-level packaged IR sensor

mass production.

Compared with traditional IR sensors, MEMS-based thermoelectric IR sensors have the advantages of small size, light weight, no cooling requirement, low noise, and simple interface circuit. Thus, they have extensive application potential in the military and civil fields. Although thermoelectric IR sensors are not as sensitive as bolometers and pyroelectric detectors, they are more ideal in many applications because of their reliable characteristics and excellent cost-performance ratio.

**Acknowledgements** This work was supported by the National Natural Science Foundation of China (Grant Nos. 51675516 and 51577186).

**Open Access** This article is distributed under the terms of the Creative Commons Attribution 4.0 International License (<http://creativecommons.org/licenses/by/4.0/>), which permits unrestricted use, distribution, and reproduction in any medium, provided you give appropriate credit to the original

author(s) and the source, provide a link to the Creative Commons license, and indicate if changes were made.

## References

1. Rogalski A. Infrared Detectors. New York: Gordon and Breach Science Publishers, 2000
2. Graf A, Arndt M, Sauer M, et al. Review of micromachined thermopiles for infrared detection. *Measurement Science and Technology*, 2007, 18(7): R59–R75
3. Socher E, Bochobza-Degani O, Nemirovsky Y. Optimal performance of CMOS compatible IR thermoelectric sensors. *Journal of Microelectromechanical Systems*, 2000, 9(1): 38–46
4. Du C H, Lee C. Characterization of thermopile based on complementary metal-oxide-semiconductor (CMOS) materials and post CMOS micromachining. *Japanese Journal of Applied Physics*,

- Part 1, Regular Papers & Short Notes, 2002, 41(6B): 4340–4345
5. Xu D, Xiong B, Wang Y. Modeling of front-etched micromachined thermopile IR detector by CMOS technology. *Journal of Microelectromechanical Systems*, 2010, 19(6): 1331–1340
  6. Socher E, Bochobza-Degani O, Nemirovsky Y. Optimal design and noise considerations of CMOS compatible IR thermoelectric sensors. *Sensors and Actuators A: Physical*, 1998, 71(1–2): 107–115
  7. Socher E, Bochobza-Degani O, Nemirovsky Y. Optimal performance of CMOS compatible IR thermoelectric sensors. *Journal of Microelectromechanical Systems*, 2000, 9(1): 38–46
  8. Völklein F, Baltes H. Optimization tool for the performance parameters of thermoelectric microsensors. *Sensors and Actuators A: Physical*, 1993, 36(1): 65–71
  9. Kozlov A G. Optimization of thin-film thermoelectric radiation sensor with separate disposition of absorbing layer and comb thermoelectric transducer. *Sensors and Actuators A: Physical*, 2000, 84(3): 259–269
  10. Kozlov A G. Analytical modelling of steady-state temperature distribution in thermal microsensors using Fourier method: Part 1. Theory. *Sensors and Actuators A: Physical*, 2002, 101(3): 283–298
  11. Kozlov A G. Analytical modelling of steady-state temperature distribution in thermal microsensors using Fourier method: Part 2. Practical application. *Sensors and Actuators A: Physical*, 2002, 101(3): 299–310
  12. Kozlov A G. Frequency response model for thermal radiation microsensors. *Measurement Science and Technology*, 2009, 20(4): 045204
  13. Escriba C, Campo E, Esteve D, et al. Complete analytical modeling and analysis of micromachined thermoelectric uncooled IR sensors. *Sensors and Actuators A: Physical*, 2005, 120(1): 267–276
  14. Mattsson C G, Bertilsson K, Thungström G, et al. Thermal simulation and design optimization of a thermopile infrared detector with an SU-8 membrane. *Journal of Micromechanics and Microengineering*, 2009, 19(5): 055016
  15. Levin A. A numerical simulation tool for infrared thermopile detectors. In: *Proceedings of 24th International Conference on Thermoelectrics*. IEEE, 2005, 476–479
  16. Elbel T, Lenggenhager R, Baltes H. Model of thermoelectric radiation sensors made by CMOS and micromachining. *Sensors and Actuators A: Physical*, 1992, 35(2): 101–106
  17. Lahiji G R, Wise K D. A monolithic thermopile detector fabricated using integrated-circuit technology. In: *Proceedings of 1980 International Electron Devices Meeting*. IEEE, 1980, 26: 676–679
  18. Roncaglia A, Ferri M. Thermoelectric materials in MEMS and NEMS: A review. *Science of Advanced Materials*, 2011, 3(3): 401–419
  19. Liao C N, Chen C, Tu K N. Thermoelectric characterization of Si thin films in silicon-on-insulator wafers. *Journal of Applied Physics*, 1999, 86(6): 3204–3208
  20. Haenschke F, Kessler E, Dillner U, et al. A new high detectivity room temperature linear thermopile array with a  $D^*$  greater than  $2 \times 10^9$  cmHz<sup>1/2</sup>/W based on organic membranes. *Microsystem Technologies*, 2013, 19(12): 1927–1933
  21. Lindeberg M, Yousef H, Rödjegård H, et al. A PCB-like process for vertically configured thermopiles. *Journal of Micromechanics and Microengineering*, 2008, 18(6): 065021
  22. Kasalynas I, Adam A J L, Klaassen T O, et al. Design and performance of a room-temperature terahertz detection array for real-time imaging. *IEEE Journal of Selected Topics in Quantum Electronics*, 2008, 14(2): 363–369
  23. Müller M, Budde W, Gottfried-Gottfried R, et al. A thermoelectric infrared radiation sensor with monolithically integrated amplifier stage and temperature sensor. *Sensors and Actuators A: Physical*, 1996, 54(1–3): 601–605
  24. Sarro P M, Yashiro H, Herwaarden A W, et al. An integrated thermal infrared sensing array. *Sensors and Actuators A: Physical*, 1988, 14(2): 191–201
  25. Fonollosa J, Carmona M, Santander J, et al. Limits to the integration of filters and lenses on thermoelectric IR detectors by flip-chip techniques. *Sensors and Actuators A: Physical*, 2009, 149(1): 65–73
  26. Fonollosa J, Halford B, Fonseca L, et al. Ethylene optical spectrometer for apple ripening monitoring in controlled atmosphere store-houses. *Sensors and Actuators B: Chemical*, 2009, 136(2): 546–554
  27. Fonollosa J, Rubio R, Hartwig S, et al. Design and fabrication of silicon-based mid infrared multi-lenses for gas sensing applications. *Sensors and Actuators B: Chemical*, 2008, 132(2): 498–507
  28. Schaufelbuhl A, Schneeberger N, Munch U, et al. Uncooled low-cost thermal imager based on micromachined CMOS integrated sensor array. *Journal of Microelectromechanical Systems*, 2001, 10(4): 503–510
  29. von Arx M, Paul O, Baltes H. Test structures to measure the heat capacity of CMOS layer sandwiches. *IEEE Transactions on Semiconductor Manufacturing*, 1998, 11(2): 217–224
  30. Baltes H, Paul O, Brand O. Micromachined thermally based CMOS microsensors. *Proceedings of the IEEE*, 1998, 86(8): 1660–1678
  31. Lenggenhager R, Baltes H, Peer J, et al. Thermoelectric infrared sensors by CMOS technology. *IEEE Electron Device Letters*, 1992, 13(9): 454–456
  32. Eriguchi K, Ono K. Quantitative and comparative characterizations of plasma process-induced damage in advanced metal-oxide-semiconductor devices. *Journal of Physics D: Applied Physics*, 2008, 41(2): 024002
  33. Li T, Liu Y, Zhou P, et al. High yield front-etched structure for CMOS compatible IR detector. In: *Proceedings of IEEE Sensors*. IEEE, 2007, 500–502
  34. Xu D, Xiong B, Wang Y. Design, fabrication and characterization of front-etched micromachined thermopile for IR detection. *Journal of Micromechanics and Microengineering*, 2010, 20(11): 115004
  35. Xu D, Xiong B, Wu G, et al. Isotropic silicon etching with XeF<sub>2</sub> gas for wafer-level micromachining applications. *Journal of Microelectromechanical Systems*, 2012, 21(6): 1436–1444
  36. Xu D, Xiong B, Wang Y, et al. Integrated micromachined thermopile IR detectors with an XeF<sub>2</sub> dry-etching process. *Journal of Micromechanics and Microengineering*, 2009, 19(12): 125003
  37. Xu D, Xiong B, Wu G, et al. Uncooled thermoelectric infrared sensor with advanced micromachining. *IEEE Sensors Journal*, 2012, 12(6): 2014–2023
  38. Roncaglia A, Mancarella F, Cardinali G C. CMOS-compatible fabrication of thermopiles with high sensitivity in the 3–5 μm atmospheric window. *Sensors and Actuators B: Chemical*, 2007, 125(1): 214–223

39. Hirota M, Nakajima Y, Saito M, et al. 120×90 element thermoelectric infrared focal plane array with precisely patterned Au-black absorber. *Sensors and Actuators A: Physical*, 2007, 135(1): 146–151
40. Chen X, Tang J, Xu G, et al. Process development of a novel wafer level packaging with TSV applied in high-frequency range transmission. *Microsystem Technologies*, 2013, 19(4): 483–491
41. Chen X, Xu G, Luo L. Development of seed layer deposition and fast copper electroplating into deep microvias for three-dimension integration. *Micro & Nano Letters*, 2013, 8(8): 191–192
42. Chen X, Yan P, Tang J, et al. Development of wafer level glass frit bonding by using barrier trench technology and precision screen printing. *Microelectronic Engineering*, 2012, 100(100): 6–11
43. Xu D, Jing E, Xiong B, et al. Wafer-level vacuum packaging of micromachined thermoelectric IR sensors. *IEEE Transactions on Advanced Packaging*, 2010, 33(4): 904–911
44. Xu D, Xiong B, Wang Y. Micromachined thermopile IR detector module with high performance. *IEEE Photonics Technology Letters*, 2011, 23(3): 149–151